The Astrophysical Journal, 612:375–388, 2004 September 1

THE BRIGHTEST PULSES IN THE UNIVERSE: MULTIFREQUENCY OBSERVATIONS OF THE CRAB PULSAR'S GIANT PULSES

J. M. Cordes
Department of Astronomy and National Astronomy and Ionosphere Center, Cornell University, Ithaca, NY 14853; cordes@astro.cornell.edu

N. D. R. Bhat
Massachusetts Institute of Technology, Haystack Observatory, Westford, MA 01886; rbhat@haystack.mit.edu

T. H. Hankins
Department of Physics, New Mexico Institute of Mining and Technology, 333 Workman Center, 801 Leroy Place, Socorro, NM 87801; thankins@nrao.edu

M. A. McLaughlin
Jodrell Bank Observatory, University of Manchester, Macclesfield, Cheshire SK11 9DL, UK; mclaughl@jb.man.ac.uk

and

J. Kern
Department of Physics, New Mexico Institute of Mining and Technology, 333 Workman Center, 801 Leroy Place, Socorro, NM 87801; jkern@nrao.edu
Received 2003 May 11; accepted 2004 May 3

ABSTRACT

We analyze the Crab pulsar at 10 frequencies from 0.43 to 8.8 GHz using data obtained at the Arecibo Observatory and report the spectral dependence of all pulse components and the rate of occurrence of large-amplitude "giant" pulses. Giant pulses occur only in the main and interpulse components that are manifest from radio frequencies to gamma-ray energies (known as the "P1" and "P2" components in the high-energy literature). Individual giant pulses reach brightness temperatures of at least 10^{32} K in our data, which do not resolve the narrowest pulses, and are known to reach 10^{37} K in nanosecond-resolution observations (Hankins et al. 2003). The Crab pulsar's pulses are therefore the brightest known in the observable universe. As such, they represent an important milestone for theories of the pulsar emission mechanism to explain. In addition, their short durations allow them to serve as especially sensitive probes of the Crab Nebula and the interstellar medium. We identify and quantify frequency structure in individual giant pulses using a scintillated, amplitude-modulated, polarized shot-noise (SAMPSN) model. The frequency structure associated with multipath propagation decorrelates on a timescale $\sim$25 s at 1.5 GHz. To produce this timescale requires multipath propagation to be strongly influenced by material within the Crab Nebula. We also show that some frequency structure decorrelates rapidly, on timescales less than one spin period, as would be expected from the shot-noise pattern of nanosecond-duration pulses emitted by the pulsar. We discuss the detectability of individual giant pulses as a function of frequency and provenance. Taking into account the Crab pulsar's locality inside a bright supernova remnant, we conclude that the brightest pulse in a typical 1 hr observation would be most easily detectable in our lowest frequency band (0.43 GHz) to a distance $\sim$1.6 Mpc at 5 σ. We also discuss the detection of such pulses using future instruments such as LOFAR and the SKA.

Subject headings: ISM: individual (Crab Nebula) — pulsars: individual (Crab Pulsar) — supernova remnants

Online material: color figures

1. INTRODUCTION

Giant pulses from the Crab pulsar are long known (Staelin & Reifenstein 1968) but remain enigmatic tools for probing the pulsar emission mechanism. Recent work has established that giant-pulse fluctuations are most likely associated with changes in the coherence of the radio emission (Lundgren et al. 1995), that giant pulses are broadband, extending over at least several hundred megahertz (Sallmen et al. 1999), and that they are superpositions of extremely narrow nanosecond-duration structures (Hankins et al. 2003). Giant pulses from the Crab pulsar have the largest implied brightness temperature of any known astrophysical source. A simple estimate for the brightness temperature, based on the light-travel size and ignoring relativistic dilation, is

$$T_b = \frac{S_\nu}{2k}\left(\frac{D}{\nu\Delta t}\right)^2 = \left(10^{30.1}\ \mathrm{K}\right) S_\nu(\mathrm{Jy})\left(\nu_{\mathrm{GHz}}\Delta t_{\mu\mathrm{s}}\right)^{-2}\left(\frac{D}{2\ \mathrm{kpc}}\right)^2, \qquad (1)$$

where S_ν is the peak flux density at frequency ν, D is the distance, k is Boltzmann's constant, and Δt is the pulse width. For observed peak amplitudes and pulse widths (e.g., 10^3 Jy at 5 GHz with $\Delta t = 2$ ns; Hankins et al. 2003), T_b ranges to as high as 10^{37} K.

In this paper we are concerned with the occurrence of giant pulses as a function of frequency and also where they occur as a function of pulse phase. We also establish the properties

TABLE 1
OBSERVATIONAL PARAMETERS

ν (GHz)	MJD	T[a] (hr)	B (MHz)	Δt (μs)	$\Delta\nu$ (MHz)	$\Delta t_{\rm DM}$ (μs)	$S_{\rm sys}$[b] (Jy)
0.430.....	52304	1.0	12.5	128	0.024	145	1262
1.180.....	52277	1.2	100	100	0.781	224	309
1.475.....	52277	1.2	100	100	0.781	115	291
2.150.....	52304–52306	1.3	100	32	1.562	74	79
2.330.....	52315	1.0	100	32	1.562	58	78
2.850.....	52306	1.0	100	32	1.562	32	74
3.500.....	52398–52412	3.5	100	64	1.562	64	41
4.150.....	52295–52337	2.9	100	32	3.125	21	20
5.500.....	52336–52411	2.3	100	32	3.125	9	20
8.600–8.800....	52398–52414	3.1	100	16	3.125	2	22

[a] T is the total time of analyzed data, whether the pulsar was detected or not.
[b] $S_{\rm sys}$ includes the contribution from the Crab Nebula that takes into account flux dilution by the telescope beam.

of the Crab pulsar's emission so that we can estimate the detectability of giant pulse emitters from other galaxies. Detections of such objects would enable studies of pulsar populations in those galaxies and use of the pulses to probe the interstellar medium (ISM) in those galaxies, as well as the intervening intergalactic medium. In addition, the Crab pulsar may serve as a prototype of intense, coherent emission from other classes of high-energy objects that may share a similar physical configuration, namely, a collimated flow of relativistic particles. As such, the Crab pulsar may signify the presence of other source classes in the transient radio universe that could be targets for proposed wide-field telescopes such as the Low-Frequency Array (LOFAR) and the Square Kilometer Array (SKA).

In § 2 we discuss the observations and issues pertaining to the strong background from the Crab Nebula and to the role of scintillation modulations associated with multipath propagation through the ISM and the Crab Nebula. Average profiles and giant-pulse profiles are discussed in § 3 and timing and amplitude statistics in § 4.

Detectability of giant pulses in other galaxies is summarized in § 6, and we conclude the paper in § 7. In the Appendix we discuss frequency structure caused by intrinsic pulse structure and by scintillation.

2. OBSERVATIONS

The Crab pulsar was observed at the Arecibo Observatory in 2002 January to March and May using receivers in the Gregorian optical path. Analog signals were analyzed with a fast-dump, real-time correlator system, the Wideband Arecibo Pulsar Processor[1] (WAPP), which outputs a data stream of correlation functions at specified time intervals. The number of correlation lags (and hence the number of channels across a choice of bandwidths after Fourier transformation) is selectable. The total bandwidth used was 100 MHz for all but 0.43 GHz, where we used 12.5 MHz. We optimized the time resolution by matching the dump time between correlations with the dispersion smearing time across individual channels, subject to a constraint on the overall data rate that could be recorded, $\lesssim$20 Mbytes s^{-1}. Table 1 gives the observing parameters: observing frequency, ν (GHz); modified Julian date (MJD); total time, T (hr), of acquired data; total bandwidth, B (MHz); sample interval, Δt (μs); channel bandwidth, $\Delta\nu$ (MHz); dispersion smearing across a single channel, $\Delta t_{\rm DM} = (8.3\ \mu{\rm s}){\rm DM}\Delta\nu\nu^{-3}$; and the mean system noise, $S_{\rm sys}$, expressed in Jy. We used a dispersion measure, DM = 56.7910 pc cm^{-3}, to dedisperse the data.

Processing consisted of (1) Fourier transforming the correlation functions for each of two polarization channels, (2) summing the resultant spectra for the two polarizations, (3) dedispersing by summing over frequency channels while taking into account time delays associated with plasma dispersion in the ISM, (4) averaging the time series synchronously with the pulsar period to form a standard intensity profile, (5) identifying individual giant pulses and their occurrence times by selecting intensity samples that exceeded the off-pulse mean by 5 σ, (6) synchronously averaging the individual giant pulses to form a histogram of giant pulses versus pulse phase, and (7) aligning average profiles and individual giant pulse profiles in pulse phase by using TEMPO and a spin model for the Crab pulsar. We also used TEMPO to perform an arrival time analysis on individual giant pulses, as discussed in § 4. For the TEMPO analysis, we used timing models from the Jodrell Bank timing program.[2]

The procedure for finding giant pulses followed that of Cordes & McLaughlin (2003). The dedispersed time series was first analyzed with the original time resolution and then progressively smoothed and decimated by factors of 2 in order to approximately match filter to pulses with different widths. In the end, most pulses were optimally detected with no smoothing or only one level of smoothing, as is consistent with the known properties of giant pulses and average profiles (Moffett & Hankins 1996; Sallmen et al. 1999). The 5 σ threshold we have used to identify giant pulses may be compared with the signal-to-noise ratios (S/Ns) of ordinary pulses (defined as the ratio of pulse peak to rms noise): S/N declines from $\sim$2 at 0.43 GHz to $\sim$0.03 at 8.8 GHz. These numbers, in turn, may be compared with giant pulses, which have maximum S/Ns in our data that range from $\sim 10^4$ at 0.43 GHz to a few hundred at frequencies above 1 GHz. Above a few gigahertz, these numbers vary greatly as a result of interstellar scintillation, as discussed below, causing the largest seen giant pulses to occasionally have S/N as large as 10^3 in our data. Note also that the numbers quoted are

[1] See http://www.naic.edu/~wapp.

[2] See http://www.jb.man.ac.uk/~pulsar/crab.html.

Arecibo specific because at frequencies higher than 1 GHz, the Crab Nebula becomes resolved and the system noise decreases dramatically.

2.1. *Importance of Nebular Background*

The Crab Nebula, whose flux density is $\sim 955\nu^{-0.27}$ Jy (ν in GHz; Allen 1973; Bietenholz et al. 1997), dominates the system temperature if it is not resolved by the telescope. Define the system temperature in the absence of the Crab Nebula as $T_{\rm sys_0}$ and the contribution from the Crab Nebula as $T_{\rm CN}$. Expressing these in flux density units by dividing by the telescope "gain" G (K Jy^{-1}), the total system noise level is

$$S_{\rm sys} = S_{\rm sys_0} + S_{\rm CN}. \tag{2}$$

For the Crab pulsar and Crab Nebula, the system temperature is strongly influenced by the Crab Nebula if, say, $S_{\rm CN} > \epsilon S_{\rm sys_0}$ with $\epsilon = 0.1$. For a single-dish telescope with typical system temperature $S_{\rm sys_0} = 50$ K and 60% aperture efficiency, this condition is satisfied for antenna diameters that satisfy

$$d > (17\ {\rm m})\nu^{0.13}\left(\frac{\epsilon T_{\rm sys_0}}{50\ {\rm K}}\right)^{1/2}. \tag{3}$$

For very large telescopes (either large single-dish antennas or arrays), the effective beamwidth can be smaller than the Crab Nebula, reducing its contribution to the system noise by a factor $f_\nu = \Omega_A/\Omega_{\rm CN}$, where Ω_A is the solid angle of the primary antenna beam and $\Omega_{\rm CN}$ is the solid angle of the Crab Nebula. The total system noise level is then

$$S_{\rm sys} = S_{\rm sys_0} + f_\nu S_{\rm CN}. \tag{4}$$

The characteristic diameter (geometric mean of the major and minor axes) of the Crab Nebula is approximately 5.′5. For the Arecibo telescope, our data at 0.43 GHz, with beam size equal to 11′ (FWHM), include all of the flux density of the Crab Nebula, while higher frequencies resolve out some of the flux density. The last column of Table 1 indicates our estimate of the system noise including any dilution of the Crab Nebula's contribution.

In the following, we express pulse amplitudes in terms of the mean system noise.

2.2. *Scintillations*

Diffractive interstellar scintillation (DISS) strongly influences the detectability of the pulsar in a manner that is strongly frequency dependent. The scintillation bandwidth scales with frequency as $\Delta\nu_d \propto \nu^{4.4}$, a result that follows if electron density fluctuations in the ISM follow a Kolmogorov wavenumber spectrum, as is consistent with measurements on nearby pulsars (e.g., Cordes et al. 1985).

There are three regimes that may be identified for scintillation modulations, depending on the size of the scintillation bandwidth, $\Delta\nu_d$, relative to the total bandwidth B and to the channel bandwidth $\Delta\nu$. For $\Delta\nu_d \ll \Delta\nu$, scintillations are essentially quenched because the large number of "scintles" in the bandpass causes the scintillation modulation to average out. For $\Delta\nu \lesssim \Delta\nu_d \lesssim 0.2B$, scintillations are identifiable as frequency structure in the spectrum of a strong, individual pulse; the net modulation in the dedispersed time series depends on the number of scintles across B and conforms roughly to a χ^2 distribution with $\sim 0.4B/\Delta\nu_d$ degrees of freedom. Finally, for $\Delta\nu_d \gtrsim 0.2B$, the dedispersed time series is fully modulated by DISS, with an amplitude modulation factor conforming to a one-sided exponential (so long as the scattering is still strong). The factor, $0.2B$, represents the approximate value of $\Delta\nu_d$ for which we would expect only one scintle within the total bandwidth, B. DISS shows the full modulation in going to higher frequencies until the scattering becomes weak (in the sense of phase perturbations on the Fresnel scale becoming less than 1 rad; see, e.g., Rickett 1990).

We estimate the DISS bandwidth by using the relation $2\pi\Delta\nu_d\tau_d = C_1$ (Cordes & Rickett 1998, hereafter CR98), where τ_d is the pulse-broadening time and C_1 is a constant dependent on the spectrum and spatial distribution of scattering irregularities; we adopt $C_1 = 1.05$, a value appropriate for a thin screen. The pulse-broadening time for the Crab pulsar is known to vary (e.g., Isaacman & Rankin 1977; Lyne & Thorne 1975; Backer et al. 1998, 2000; Lyne et al. 2001), ranging from about 0.28 to 1.3 ms at 0.3 GHz (Sallmen et al. 1999). Adopting $\tau_d(0.3\ {\rm GHz}) = 0.5$ ms as a reference value, we estimate $\Delta\nu_d \approx (67\ {\rm kHz})\nu^{4.4}[0.5\ {\rm ms}/\tau_d(0.3\ {\rm GHz})]$, with ν in GHz. Using this expression, we expect that the dedispersed pulse will show fully modulated scintillations (i.e., after summing over the 100 MHz bandwidth) for $\nu \gtrsim 3.6$ GHz.

We found the mean pulsar flux density (averaged over a few minutes) to be heavily modulated on timescales as short as 5 minutes at frequencies $\gtrsim$3 GHz and nearly unchanging at lower frequencies. Such fluctuations are consistent with those expected from DISS, as we discuss in § 5. We also saw epoch-to-epoch fluctuations (timescales of 1 day and longer) that are consistent with refractive interstellar scintillations (RISSs), like those identified by Lundgren et al. (1995) at 0.8 GHz on timescales of a few days. The combination of RISS and DISS is particularly strong at 8.8 GHz where the pulsar is undetectable on many days but quite bright, in the mean, on occasional days with DISS fluctuations contributing on shorter timescales. We note that at 8.8 GHz, the diffraction bandwidth $\Delta\nu_d \approx 1$ GHz (assuming the $\nu^{4.4}$ scaling), implying that the strength of scattering (as defined in scintillation literature; see Rickett 1990) is not strong and that the DISS and RISS "branches" are not as distinct as at lower frequencies (e.g., Narayan 1992).

We point out that our measurements were made at a range of epochs, so direct comparison of giant-pulse statistics at different frequencies may be influenced by epoch-dependent effects, most likely exclusively associated with interstellar scintillations and scattering.

3. AVERAGE PROFILES

We calculated average profiles of the total intensity by summing partial sum profiles (of 3–12 minutes duration, depending on frequency) in which the largest pulse component had an S/N larger than 5 and that were unmarred by radio frequency interference (RFI).

At frequencies higher than 0.43 GHz, typically only a minority of profiles were included as a result of the effects of DISS or RFI. Likewise, profiles of giant-pulse counts were calculated using data subsets corresponding to those included in the average intensity profiles.

Figure 1 shows average intensity and giant-pulse profiles for the 10 frequencies listed in Table 1. The top panel of the pair shown for each frequency is the total intensity profile, and the bottom panel shows the giant-pulse histogram versus pulse phase, i.e., the number of giant pulses in the given pulse phase

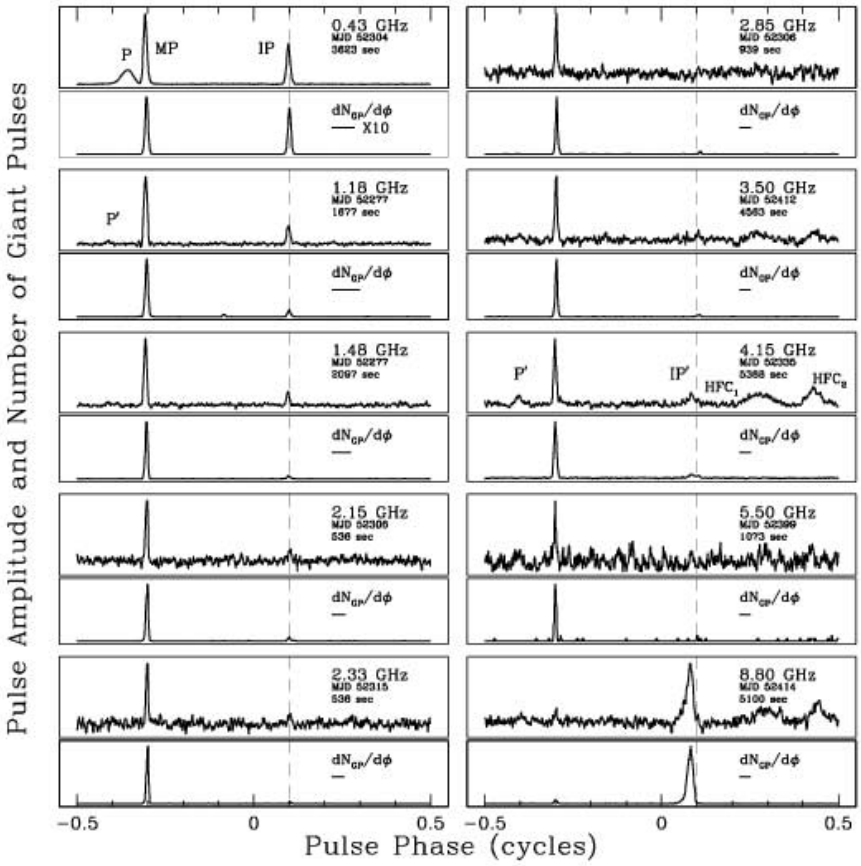

FIG. 1.—Total intensity profiles of the Crab pulsar at 10 radio frequencies. The pair of plots for each frequency is the standard average intensity profile (*top*) and a histogram of counts of giant pulses plotted against pulse phase (*bottom*). A threshold of 5 σ was used to obtain giant pulses included in the histograms. The total integration time is given in the top panel, and a horizontal bar designates the net instrumental time resolution, including the effects of dispersion smearing across individual spectrometer channels; the shown bar length is 10 times the actual length. [*See the electronic edition of the Journal for a color version of this figure*.]

bin that are above threshold (5 σ). In some of the panels we designate features in the pulse profile, including low-frequency precursor pulse (P), main pulse (MP), interpulse (IP), an intermediate-frequency precursor component (P′; referred to by Moffett & Hankins 1996 as a ''low-frequency component''), a shifted interpulse component appearing at mid- to high frequencies (IP′), and two high-frequency components (HFC1 and HFC2) that were first identified by Moffett & Hankins (1996).

We point out the following features of the set of profiles:

1. The pulsar is more readily detectable in its single giant pulses than in the average pulse at all frequencies. This is manifest by the larger S/N in the histogram plots compared to the average profile plots in Figure 1.

2. There is strong evolution of the relative strength of MP and IP as a function of frequency. The ratio of peak IP to peak MP steadily declines from 0.43 to 2 GHz, stays low from 2.5 to 3.5 GHz, and rises at higher frequencies so that the IP is much stronger than the MP at 8.8 GHz.

3. At 4.15 GHz, IP′ appears approximately 0.03 cycles before the location of the lower frequency IP and becomes very strong relative to the MP at 8.8 GHz.

4. At frequencies of 3.5 GHz and higher two new components, HFC1 and HFC2, appear and persist up to the highest frequency we used (8.8 GHz).

5. It is unclear if the HFC1 and HFC2 components are present at 2.15, 2.33, and 2.85 GHz as a result of the low S/N of those profiles, which derives from the short integration times and the effects of scintillations.

6. Giant pulses occur only in MP, IP, and IP′. For this reason we conclude that IP and IP′ are probably associated with the same physical emitting region or beam in the pulsar.

7. There is more scatter in the pulse phase of the interpulse at high frequencies, manifested in the broader width of the interpulse component. As discussed in § 4, at 8.8 GHz the phase residuals appear to show a two-component distribution, one centered on $\phi = 0.38$ cycles, the other representing giant pulses skewed toward smaller phases.

4. AMPLITUDE AND TIMING STATISTICS OF GIANT PULSES

Table 2 gives the frequency and total time span used in our analysis in columns (1) and (2); column (3) gives the mean main pulse–to–interpulse phase difference; column (4) gives the ratio of the numbers of detected interpulses and main pulses; and column (5) gives the detection rate for events found at 8 σ or higher.[3] At 0.43 GHz, about 1 in 10 pulses is detected above this level. We emphasize that the detection rate is epoch dependent as a result of scintillation modulations. Slow, refractive scintillations affect the rates at all frequencies,

[3] Here we have used an 8 σ rather than a 5 σ threshold to keep arrival time errors small.

TABLE 2
GIANT PULSE AMPLITUDE AND TIMING STATISTICS

ν (GHz) (1)	T[a] (hr) (2)	$\overline{\phi}_{ip} - \overline{\phi}_{mp}$ (cycles) (3)	N_{ip}/N_{mp} (4)	$\dot{N}_{GP}$[b] (s^{-1}) (5)
0.430	1.0	0.4032 ± 10^{-4}	0.56	3.3
1.180	0.47	0.402 ± 0.001	0.05	0.51
1.475	0.58	0.402 ± 0.001	0.05	0.31
2.150	0.15	0.403 ± 0.002	0.07	0.25
2.330	0.15	0.403 ± 0.002	0.08	0.17
2.850	0.26	0.404 ± 0.003	0.05	0.11
3.500	1.27	0.402 ± 0.002	0.04	0.12
4.150	1.49	0.394 ± 0.002	0.10	0.31
5.500[c]	0.30	...	...	0.02
8.800	1.42	0.380 ± 0.001	27	0.44

[a] T represents the total time included in the average profiles of Fig. 1, which represents only the high-S/N and RFI-free subset of the overall data.
[b] For frequencies $\gtrsim$3 GHz, the number of detected giant pulses varies significantly because diffractive interstellar scintillation strongly modulates their amplitudes. Numbers are therefore biased because many observations yielded no detection of the pulsar. Refractive scintillation also alters the detection rate at all frequencies.
[c] At 5 GHz, too few interpulses are detected to allow meaningful estimates of the MP-to-IP phase offset and number ratio.

while fast diffractive scintillations are particularly important at frequencies above 3 GHz. The 8.8 GHz results apply to a particular day when the scintillation modulation boosted intensities far above their normal level. The main pulse–to–interpulse phase difference varies systematically with frequency, remaining constant with frequency (within errors) from 0.43 to 3.5 GHz and then declining with increasing frequency up to 8.8 GHz. This variation in calculated phase difference corresponds to the shift from IP to IP′.

While the absolute rates of giant-pulse detection are influenced by scintillations and resolution of the Crab Nebula by the telescope beam, the ratio of giant-pulse to average flux density is not. At 0.43 GHz, $S_{GP}/\langle S \rangle$ has a median value of 8 and a peak of 840 (in our data). Going to higher frequencies, there is an increasing trend for the median and peak values for this ratio: 18 and 420 for 1.2 GHz, 29 and 510 for 1.5 GHz, 83 and 1580 for 2.3 GHz, 127 and 2390 for 3.5 GHz, 250 and 4700 for 5.0 GHz, and 533 and 5260 for 8.8 GHz. These results imply that giant-pulse amplitudes decrease with frequency more slowly than do average-pulse amplitudes.

Our detections of giant pulses were made using receiver bandwidths of 100 MHz at frequencies above 1 GHz and 12.5 MHz at 430 MHz. Individual giant pulses extend in frequency by at least these bandwidths, but the data discussed here cannot establish the actual bandwidth of individual pulses. Simultaneous measurements at 0.6 and 1.4 GHz demonstrate that the radiation bandwidth is at least 0.8 GHz (Sallmen et al. 1999).

Figures 2 and 3 show histograms of S/N at 0.43 and 8.8 GHz for the main and interpulse components specified in Figure 1. We include only pulses with $S/N > 8$ in order to provide consistency with the timing analysis discussed below, where we use an 8 σ threshold for the purpose of obtaining timing residuals minimally influenced by noise. Traditionally, giant-pulse amplitude distributions have been characterized as power laws (e.g., Argyle & Gower 1972; Lundgren et al. 1995). The histograms shown here have roughly power-law segments to their distributions, but there are outlier pulses at especially high S/N at both frequencies. Roughly, a power law with

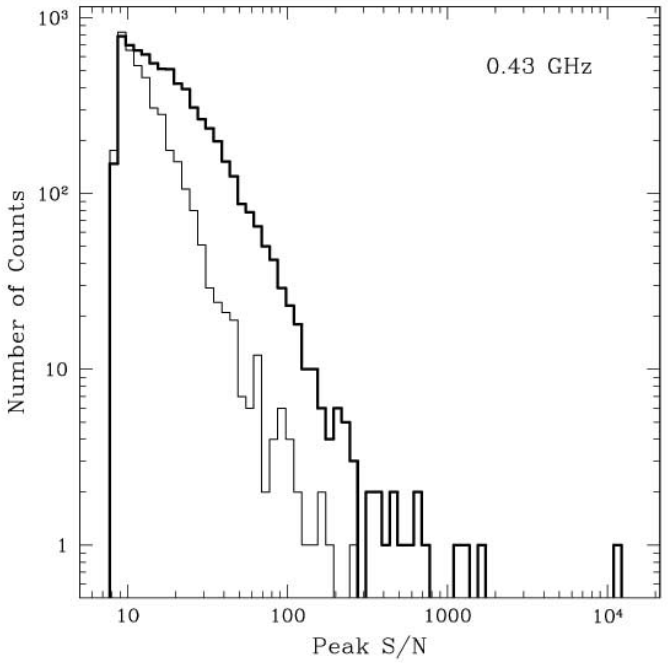

FIG. 2.—Histogram of giant-pulse peak amplitudes at 0.43 GHz. The lower curve is for the interpulse, and the upper curve is for the main pulse. [*See the electronic edition of the Journal for a color version of this figure*.]

slope ≈ -2.3 can be drawn through the MP histogram at 0.43 GHz in Figure 2 and a slope ≈ -2.9 at 8.8 GHz in Figure 3. These can be compared with slopes of approximately -2.5 at 0.146 GHz (Argyle & Gower 1972) and -3.6 at 0.812 GHz (Lundgren et al. 1995). Overall there thus appears to be steepening of the histogram in going from low to high frequencies. Remarkably, the largest pulse at 0.43 GHz has

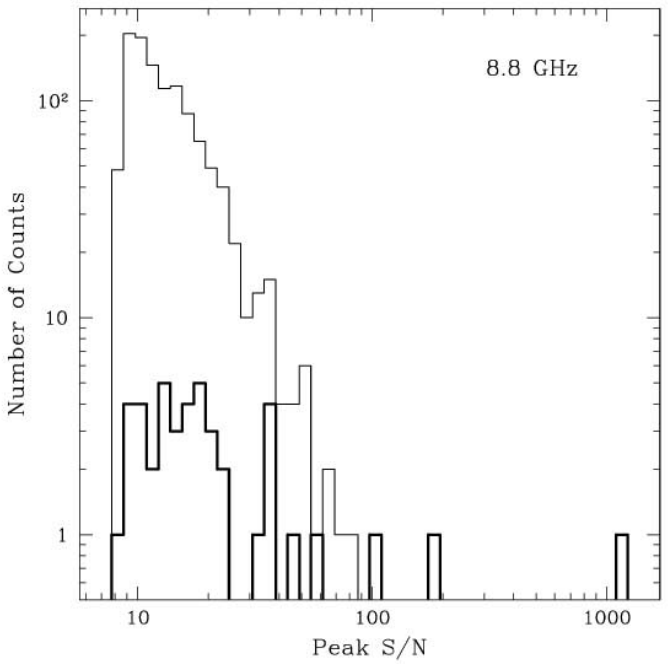

FIG. 3.—Histogram of giant-pulse peak amplitudes at 8.8 GHz. The upper curve is for the interpulse, and the lower curve is for the main pulse. Contrary to lower frequency data, interpulses are much more common than main pulses at 8.8 GHz. [*See the electronic edition of the Journal for a color version of this figure*.]

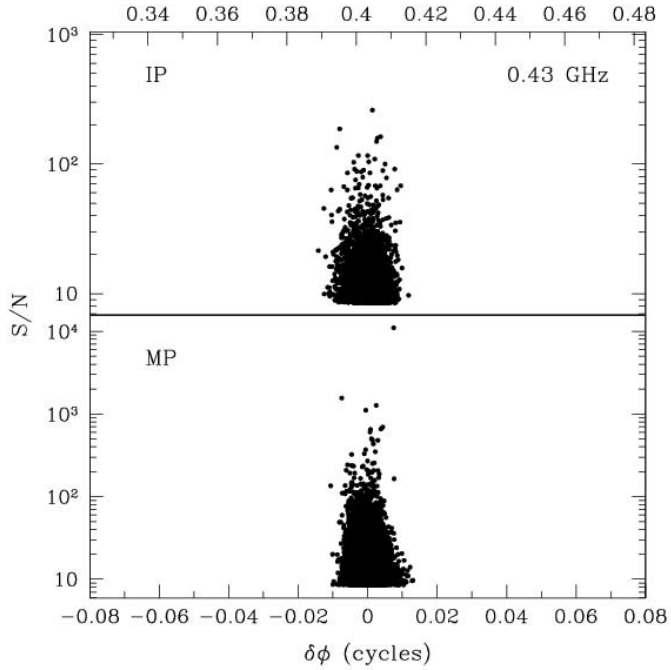

FIG. 4.—Scatter plots of S/N and pulse phase for 0.43 MHz for the interpulse (IP′) and main pulse (MP). The mean main pulse phase is defined to be zero.

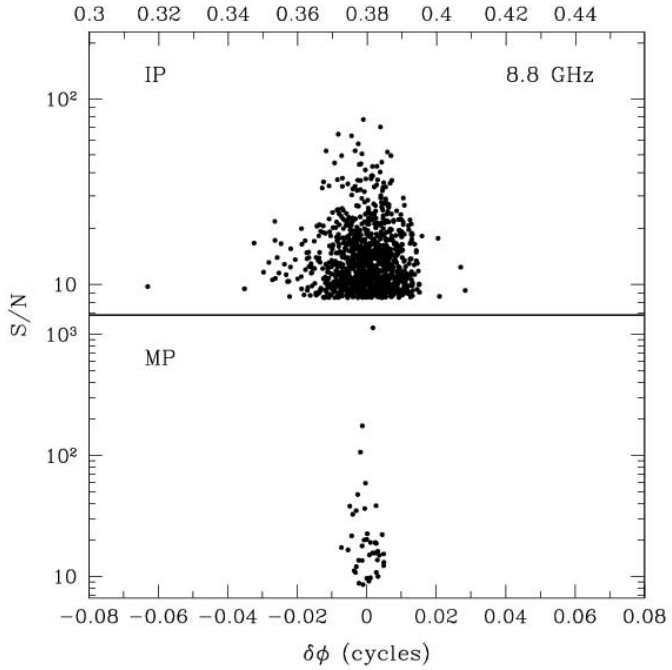

FIG. 5.—Scatter plots of S/N and pulse phase residual for 8.8 GHz for the interpulse (IP) and main pulse (MP).

S/N $\sim 1.1\times10^4$, which is inconsistent with the probability implied by the power law at lower S/N. We suggest that this pulse is an example of a *supergiant* pulse. The same is true at 8.8 GHz, where giant pulses in the interpulse region are dominant in number but the largest pulse appears in the main pulse component and is 10 times larger than the largest interpulse giant pulse. Conceivably, the largest pulses seen at 0.43 and 8.8 GHz are statistical flukes. The extensive observations of Lundgren et al. (1995) at 0.8 GHz do not indicate the presence of a gap between the brightest and typical giant pulses.

The joint statistics of timing phase residuals and pulse amplitudes (expressed as S/N) are shown in Figures 4 and 5 for the main pulse and interpulse separately. At the lower frequency (0.43 GHz), the main pulse phase residuals show a skewed distribution toward larger phases. At 8.8 GHz, the distribution of phase residuals in the interpulse is much broader than in the main pulse and in either component at 0.43 GHz. This trend is consistent with the appearance of the average profiles in Figure 1. At 8.8 GHz, the giant interpulses showing the most negative phase residuals tend to be weaker than the average. Otherwise, there is no evidence for a strong relationship between amplitude and phase residual.

5. SCINTILLATIONS AND SPECTRAL FLUCTUATIONS

From the discussion in § 2.2, we estimate that the scintillation bandwidth will range from about 2 kHz at 0.43 GHz to about 1 GHz at 8.8 GHz if we assume a scaling $\Delta\nu_d \propto \nu^{4.4}$. Previous work also suggests that at any epoch the actual scintillation bandwidth could vary by a factor of a few about these values. Such variations are due to the stochastic nature of the process but also are caused by refractive modification of the diffraction parameters (e.g., Rickett 1990). At our lowest frequency, 0.43 GHz, the DISS bandwidth is about 1/10 the channel bandwidth (see Table 1). Thus, the brightest features in the frequency-time data are expected to be diminished by the smoothing implied by the spectrometer resolution. At our highest frequency, 8.8 GHz, the predicted DISS bandwidth is a factor of 8 smaller than the center frequency, signifying that scintillations are in the transition regime between strong and weak scattering. In the transition regime, we expect deep modulations as in the strong scattering regime, but with different statistics, and, according to our estimate, they will be highly correlated across our 100 MHz bandwidth.

Of course, our predictions for DISS bandwidth require some caveats. First, our data were obtained over a 0.4 yr period over which time the scattering strength undoubtedly varied, probably yielding an implied pulse-broadening time at 0.43 GHz different from the value we have assumed (100 μs). Second, the scaling with frequency of the DISS quantities may depart from that which has been identified along other lines of sight (LOSs) in the ISM. The scaling with the 4.4 exponent has been established for pulsars with small dispersion measures (DMs), while a few objects show a weaker scaling as ν^4. Recent work on high-DM pulsars (Löhmer et al. 2001; Bhat et al. 2003) indicates that the pulse-broadening time may vary as weakly as ν^{-3} (and the scintillation bandwidth thus as ν^3). However, it is also clear from Bhat et al. (2003) that empirical determinations of the exponent are sensitive to assumptions about the form of the pulse-broadening function fitted to the data and how it interacts with the assumed intrinsic pulse shape of the pulsar. Nonetheless, despite these uncertainties, evidence suggests that the pulse broadening from the Crab pulsar not only is highly variable but often exceeds the predictions based on lower frequencies using either of the strong scaling laws, $\Delta\nu_d \propto \nu^4$ or $\nu^{4.4}$. Possible interpretations include contributions from scattering within the pulsar magnetosphere (Hankins & Moffett 1998) or from scattering regions within the Crab Nebula that are bounded spatially (Cordes & Lazio 2001). Spatially bounded scattering regions can generate scattering times that scale with frequency differently than with an exponent of 4 or 4.4.

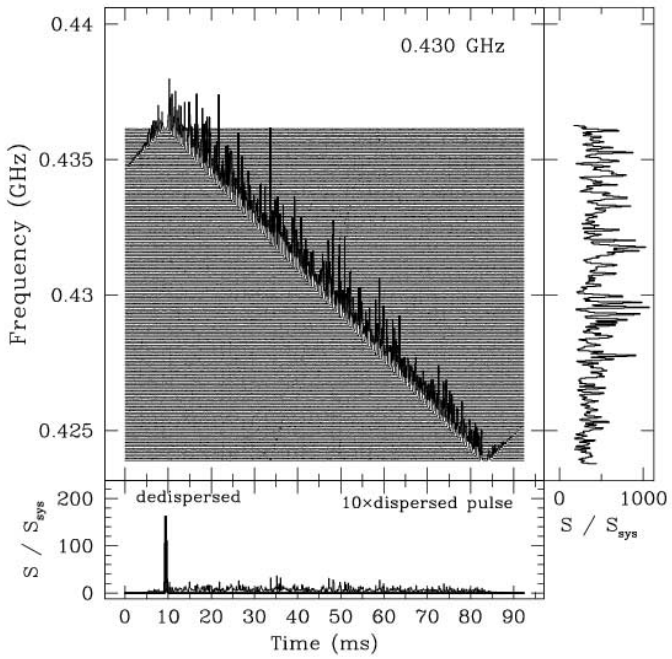

FIG. 6.—Plot of intensity against time and frequency, showing a single dispersed pulse as it arrives at different frequencies centered on 0.43 GHz. The right panel shows the pulse amplitude vs. frequency, while the bottom panel shows the pulse shape with and without compensating for dispersion delays. The sharp pulse at about 10 ms is the dedispersed pulse, while the noiselike trace extending over most of the time axis is the dispersed pulse (multiplied by 10). This pulse is the largest in 1 hr of data and has S/N $\sim 1.1\times10^4$ and a pulse peak that is 130 times the flux density of the Crab Nebula, or $\sim$155 kJy. Note that the segments at either end of the bandpass have arrival time variations with frequency that are opposite to those seen at most frequencies; this is caused by aliasing of the signal. [*See the electronic edition of the Journal for a color version of this figure*.]

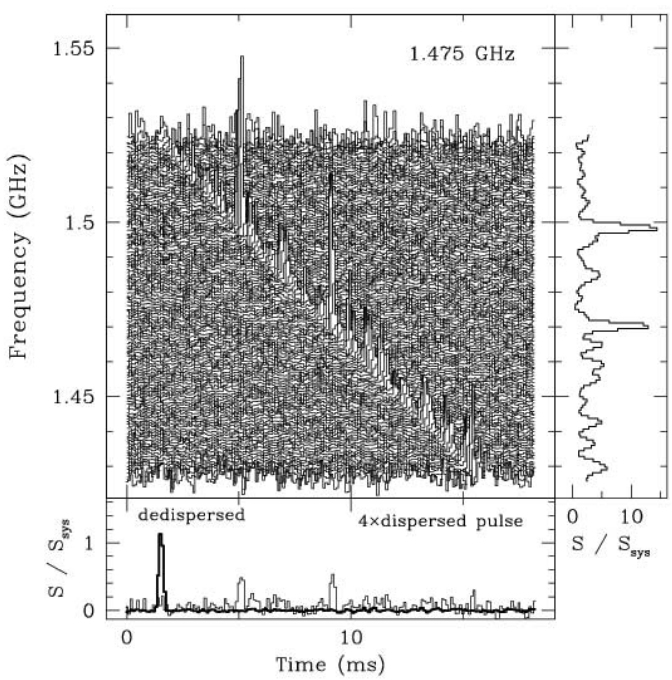

FIG. 7.—Same as Fig. 6, but for a single pulse at 1.475 GHz. This pulse is the largest in 1 hr of data and has S/N $\sim$225 and a pulse peak that is 1.2 times the mean system noise, or $\sim$1.03 kJy. Note that individual scintles in the spectrum reach 14 times S_{sys}, or 4.1 kJy. [*See the electronic edition of the Journal for a color version of this figure*.]

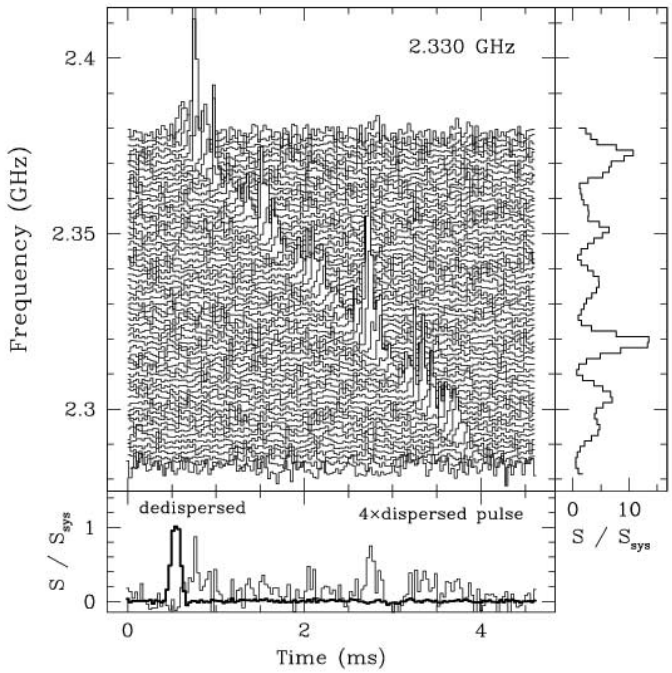

FIG. 8.—Same as Fig. 6, but for a single pulse at 2.33 GHz. This pulse is the largest in 1 hr of data and has S/N $\sim$161, a pulse peak that is $1.1S_{sys}$, and a scintillation peak $\sim 12S_{sys}$. At this frequency the telescope beam resolves the Crab Nebula, so the peak flux densities are $\sim$86 and $\sim$936 Jy in the dedispersed pulse and spectrum, respectively. [*See the electronic edition of the Journal for a color version of this figure*.]

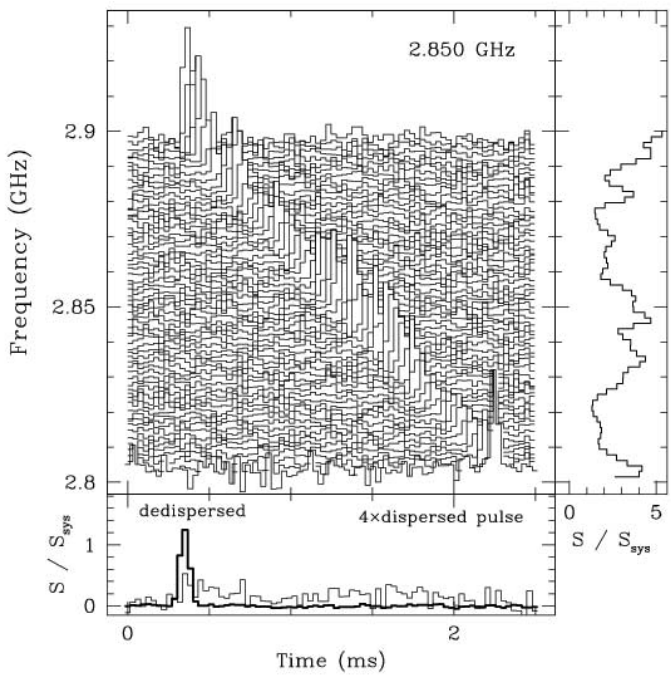

FIG. 9.—Same as Fig. 6, but for a single pulse at 2.85 GHz. This pulse is the largest in 1 hr of data and has S/N $\sim$111, a pulse peak that is $1.2S_{sys}$, and a scintillation peak $\sim 4.5S_{sys}$. At this frequency the telescope beam resolves the Crab Nebula, so the peak flux densities are $\sim$89 and $\sim$333 Jy in the dedispersed pulse and spectrum, respectively. [*See the electronic edition of the Journal for a color version of this figure*.]

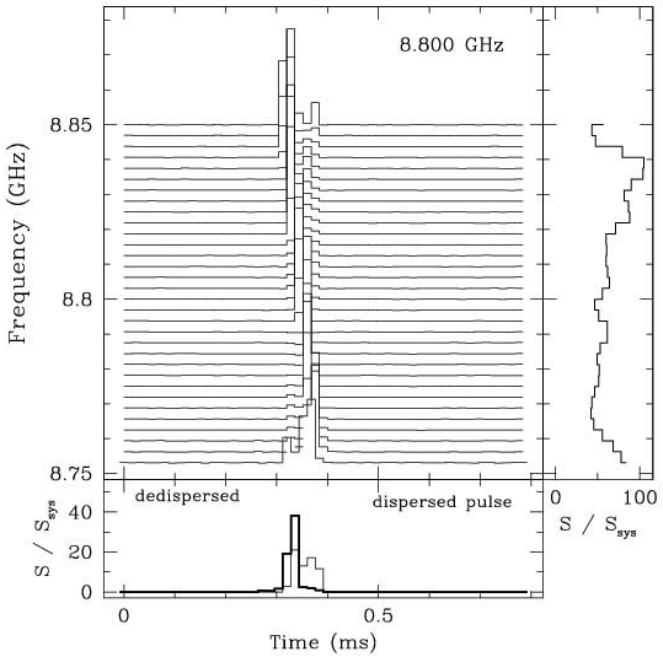

FIG. 10.—Plot of intensity against time and frequency, showing a single dispersed pulse as it arrives at different frequencies centered on 8.8 GHz. The right panel shows the pulse amplitude vs. frequency, while the bottom panel shows the pulse shape with and without compensating for dispersion delays. This pulse is the largest in 1 hr of data and has S/N $\sim 1.3\times10^3$, a pulse peak that is $\sim 40 S_{\rm sys}$, and a spectral peak $\sim 100 S_{\rm sys}$. At this frequency the telescope beam resolves the Crab Nebula. The peak flux densities are ~880 and $\sim 2.2\times10^3$ Jy in the dedispersed pulse and spectrum, respectively. [*See the electronic edition of the Journal for a color version of this figure.*]

In Figures 6–10 we show plots of the pulsed flux for single giant pulses in the frequency-time plane, the pulse shape obtained by summing over frequency both with and without compensation for dispersion delays, and the spectrum of the pulse.

At 0.43 GHz, the pulse is easily detected even without dedispersion as a result of the high S/N. Structure in the spectrum is quite spiky and is associated with individual scintles caused by DISS. This is so, in spite of the fact that the DISS bandwidth is substantially smaller than the channel bandwidth, because the spacing between scintles is quite large. DISS in the strong scattering regime is exponentially distributed, with an ensemble average mean modulation of unity. Consistent with the statistics is the estimate that the number of strong scintles within a bandwidth B is

$$N_\nu \approx 1 + 0.2B/\Delta\nu_d. \quad (5)$$

As can be seen in the right panel of Figure 6, the minimum spectral values away from the bandpass edges are well offset from zero, signifying that the overall modulation is less than the 100% expected from exponential DISS statistics, consistent with the smoothing of scintles that occurs in the process of channelizing the data.

By comparison, plots of giant pulses at 1.5 and 2.4 GHz (Figs. 7 and 8) show minimum spectral values nearly equal to zero flux density, consistent with the larger, nearly resolved or resolved scintillation structure expected at those frequencies. At 2.85 GHz, the minimum spectral values are well above zero, signifying that the DISS bandwidth is large enough that only one or two scintles are expected across the band. At 8.8 GHz (Fig. 10), the modulation of the flux across the bandpass has a much different character, as expected if $\Delta\nu_d \gg B$, where $B = 100$ MHz.

5.1. *Scintillation Bandwidths*

We estimate the scintillation bandwidth by calculating the intensity autocorrelation function, $A(\delta\nu) = \langle I(t,\ \nu)I(t,\ \nu+\delta\nu)\rangle$, for the spectrum of each giant pulse and summing over giant pulses. For this analysis, we used giant pulses with S/N > 20 in the dedispersed pulse. Scintillation structure is unresolved at frequencies below 2 GHz and is comparable to or larger than our receiver bandpass at frequencies larger than 4 GHz. Results are shown in Table 3 along with scintillation timescales, discussed in the next section, and the number of giant pulses used to estimate the parameters.

5.2. *Scintillation Timescale*

The scintillation timescale is the time for features in the diffraction pattern to transport across the LOS, combined with any reorganization of the diffraction pattern itself. These two contributions are determined by the velocities of the source and observer and any bulk motion of the intervening material, which change the sampling geometry of the diffraction pattern, combined with random velocities in the medium. Traditionally the scintillation timescale is calculated as the e^{-1} width along the time-lag axis of the two-dimensional intensity correlation function, $C(\delta\nu,\ \tau) = \langle I(t,\ \nu)I(t+\tau,\ \nu+\delta\nu)\rangle$. For strong pulsars with steady pulse emission and scintillation timescales of minutes or longer, $C(\delta\nu,\ \tau)$ can be calculated on a uniform grid of $\delta\nu$ and τ. However, for the Crab pulsar, the giant pulses allow only sporadic sampling along the time-lag axis. At most of our observing frequencies, it is difficult to establish values for Δt_d either because the DISS frequency structure is unresolved (e.g., at 0.43 GHz) or because we cannot find enough close pairs of giant pulses having adequate S/N to estimate reliably the correlation coefficient of the spectra. However, at 1.475 and 2.33 GHz, detectable pulses allow us to estimate Δt_d.

Figure 11 shows spectra for a close pair of high-S/N pulses at 1.475 GHz. While some of the features in the spectra align, it is clear that the frequency structure has decorrelated significantly. The correlation coefficient is only 0.46. If scintillations were the only source of frequency structure, this would imply an exceedingly short decorrelation time. However, some of the frequency structure is associated with the intrinsic noise of the pulsar signal. (Little structure is associated with additive radiometer noise as a result of the high S/N of 66 and 82 for the dedispersed pulses.) The intrinsic frequency structure has a frequency scale $\Delta\nu_i \approx W_A^{-1}$, where W_A is the characteristic pulse width. With $W_A \approx 100$ μs, the intrinsic structure is expected to show $\Delta\nu_i \approx 10$ kHz, much narrower

TABLE 3
SCINTILLATION PARAMETERS

ν (GHz)	$\Delta\nu_d$ (MHz)	Δt_d (s)	$N_{\rm GP}$
0.43	<0.024	...	100
1.48	<0.8	25 ± 5	180
2.33	2.3 ± 0.4	35 ± 5	170
2.85	7 ± 2	...	60
3.50	15 ± 10	...	15

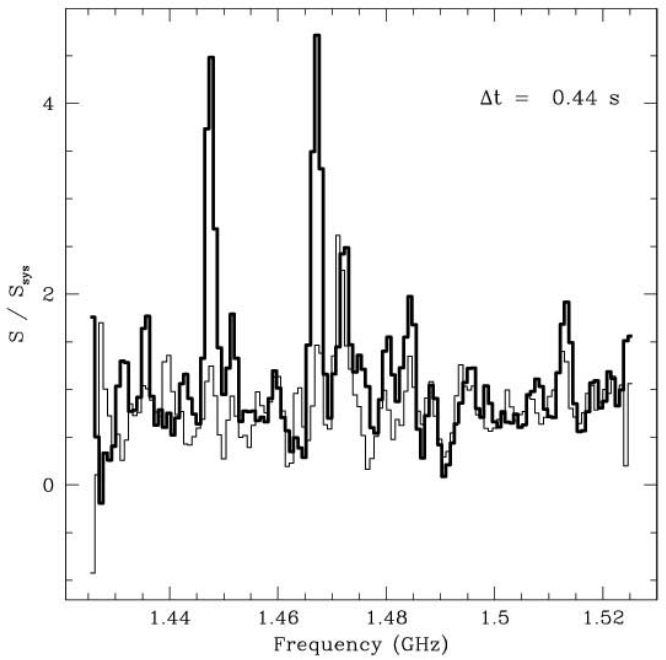

FIG. 11.—Plot showing spectra for two giant pulses spaced by $\Delta t = 0.44$ s and having S/N of 66 and 82 (defined as peak to rms in the dedispersed time series) for the curves with the thin and thick lines, respectively. The largest spectral peaks in the stronger pulse have S/N $\approx$ 100. Additive radiometer noise therefore contributes very little to the spectral structure shown here. Features in the spectra for the two pulses align in frequency but have very different amplitudes. The correlation coefficient between the two spectra is 0.46. As discussed in the Appendix, some of the frequency structure is caused by DISS, while other structure is associated with the intrinsic noise properties of the pulse. [*See the electronic edition of the Journal for a color version of this figure*.]

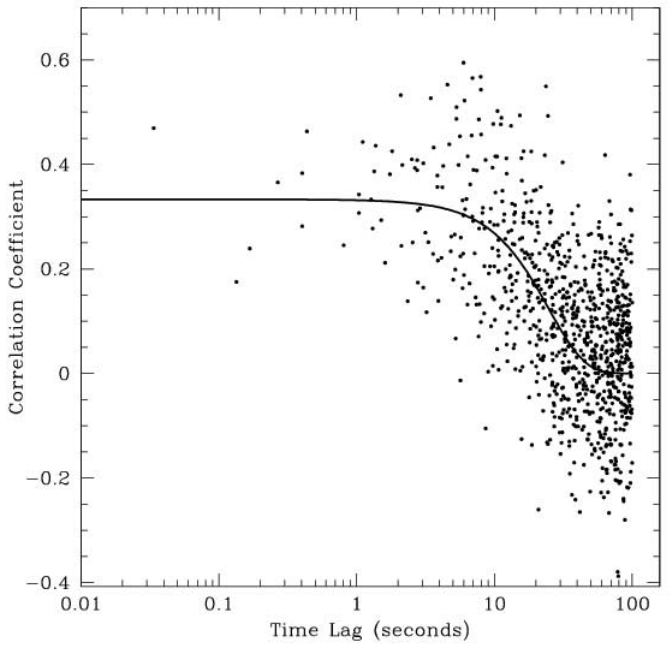

FIG. 12.—Plot of the correlation coefficient $C(\delta\nu = 0, \tau)$ vs. time lag τ between spectra of giant pulses at 1.475 GHz, where τ is the time separation between pairs of giant pulses. At this frequency, the number of close pairs is sufficient to establish that frequency structure in the spectra is correlated over short timescales, with an e^{-1} timescale $\approx 25 \pm 5$ s. The smallest lag occurs at one of the quantized values determined by the spacing of the main pulse and interpulse components. The line represents the mean correlation function expected for scintillating amplitude-modulated shot noise with a correlation time of 25 s.

than the channel bandwidth of 0.78 MHz. However, substructure within the pulse envelope comprising short-duration pulses of duration 1 μs or less would increase this scale to 1 MHz or more. Hankins et al. (2003) have identified substructure in giant pulses on these short timescales. We conclude that the intrinsic pulse structure is responsible primarily for the fast decorrelation between the pair of pulses. This conclusion is corroborated by a statistical study of a large number of pulse pairs, as follows.

Figure 12 shows the correlation coefficient $C(0, \tau)$ between a large number of pulse pairs plotted against time separation, τ. We have used only those pulses with S/N > 20 in the dedispersed pulse in order to reduce scatter in the correlation estimates from additive noise. The roll-off of the correlation coefficient at larger lags represents a correlation time, $\Delta t_d \approx 25 \pm 5$ s at 1.475 MHz. From the Appendix, we expect the asymptotic correlation coefficient (at small lags) to be $1/(2 + d_p^2)$, in the mean, under the scintillated, amplitude-modulated, polarized shot-noise (SAMPSN) model and where d_p is the degree of polarization ($\leq$1). This level is consistent with the level of correlation seen at lags $\tau \lesssim 1$ s if the pulses are typically highly polarized. Consistency of giant-pulse spectral statistics with SAMPSN implies that, typically, pulses at 1.475 GHz are composed of a large number ($\gtrsim$5) of individual shot pulses in order that the intrinsic fluctuations are Gaussian and thus contribute to the rapid decorrelation seen (see the Appendix).

A similar analysis for 2.33 GHz data yields a somewhat longer timescale (Table 3). At still higher frequencies, there are insufficient pairs of strong pulses to establish the correlation time, although we are able to estimate the scintillation bandwidth up to 3.5 GHz. At 8.8 GHz, where the scintillation bandwidth is larger than the observation bandwidth, we expect spectral modulations to derive solely from amplitude-modulated noise statistics (combined with radiometer noise), implying that the modulation index $m_I = \sigma_I/I = [(1 + d_p^2)/2]^{1/2}$ (after correction for any contribution from radiometer noise, which is negligible for the largest pulses). For the pulse displayed in Figure 10, the modulation index is only 0.29. A low modulation index suggests that the giant pulse of that figure is dominated by a single shot pulse with duration comparable to the reciprocal bandwidth, $\sim$10 ns, or that the giant pulse comprises a cluster of shot pulses with a similar width. Such results are not inconsistent with those of Hankins et al. (2003), who found nanosecond structure within individual giant pulses at 5 GHz.

5.3. *Scintillation Speed*

The effective speed with which the intensity pattern caused by multipath propagation crosses the LOS can be estimated from the scintillation bandwidth and timescale. If we assume that electron density fluctuations have a Kolmogorov spectrum and fill the LOS uniformly, the pattern speed would be (CR98)

$$V_{\mathrm{ISS},5/3,u} = A_{\mathrm{ISS},5/3,u} \frac{\sqrt{D\Delta\nu_d}}{\nu \Delta t_d}, \qquad (6)$$

with $A_{\mathrm{ISS},5/3,u} = 2.53 \times 10^4$ km s^{-1} for ν in GHz, Δt_d in s, $\Delta\nu_d$ in MHz, and D in kpc. We evaluate $V_{\mathrm{ISS},5/3,u}$ at 1.475 GHz by using the decorrelation time estimated in the previous section but by scaling the scintillation bandwidth from 2.33 GHz,

since it is unresolved at 1.475 GHz. Scaling from 2.33 GHz using $\Delta\nu_d \propto \nu^{4.4}$, we obtain $\Delta\nu_d \approx 0.31 \pm 0.05$ MHz. Using $D = 2$ kpc for the distance to the Crab Nebula, the scintillation speed is $V_{\rm ISS,5/3,u} \approx 540$ km s^{-1}. Under the assumptions leading to this estimate, $V_{\rm ISS,5/3,u}$ should be approximately equal to the transverse pulsar speed, $|\boldsymbol{V}_{p\perp}| \approx 171 \pm 28$ km s^{-1}, from a *Hubble Space Telescope* (*HST*) proper-motion measurement (Caraveo & Mignani 1999); instead, there is a factor of 3 discrepancy.

No element in the scattering geometry (pulsar, medium, or source) has a velocity as large as $V_{\rm ISS,5/3,u}$, and it is reasonable to conclude that the scattering medium is in fact not uniform along the LOS and in particular receives significant contributions from the Crab Nebula's filaments. The filaments are dense ($\sim 10^3$ cm^{-3}) and have characteristic scales $\sim 10^{16}$ cm (e.g., Sankrit et al. 1998), so that significant phase perturbations are expected at our frequencies of observation. First, we ignore the effects of the general ISM and consider filamentary scattering screens at a distance $D_s \approx 1$ pc from the pulsar. Then, using equations (13)–(18) of CR98 to correct for the geometric leveraging effects of screen(s) near the pulsar, we obtain

$$V_{\rm ISS} = W_C \left[\frac{2(D - D_s)}{D_s}\right]^{1/2} V_{\rm ISS,5/3,u} \approx 3.4\times 10^4 \left(\frac{D/D_s}{2000}\right) \text{ km s}^{-1}, \quad (7)$$

where we have used $W_C \approx 1.05$ (see Fig. 1 of CR98).

For a thin screen, the pattern speed is related physically to the velocities of the pulsar, observer, and medium as (CR98, eq. [4]) $V_{\rm ISS} = (D/D_s)|\boldsymbol{V}_{\rm eff,\perp}|$, or

$$V_{\rm ISS} = \left|\left(\frac{D}{D_s} - 1\right)\boldsymbol{V}_{p\perp} + \boldsymbol{V}_{\rm obs\perp} - \left(\frac{D}{D_s}\right)\boldsymbol{V}_{m\perp}\right|, \quad (8)$$

where $\boldsymbol{V}_{p\perp}$, $\boldsymbol{V}_{\rm obs\perp}$, and $\boldsymbol{V}_{m\perp}$ are the transverse velocities of the pulsar, observer, and medium, respectively, relative to the local standard of rest. The pulsar and medium's velocities are "boosted" by the factor $D/D_s \approx 2000$, so we may ignore the Earth's motion in the following.

Filament velocities along the LOS are $\lesssim 1500$ km s^{-1} (Fesen & Kirshner 1982). To estimate the effective transverse velocity, we consider the symmetry of filament motions and the change in geometry since the supernova explosion. Figure 13 shows the geometry under the assumption of purely radial motion by wind material (which may represent a pre-supernova wind or blast wave material). The present-day transverse velocity of the pulsar implies transverse wind/filament velocities $\boldsymbol{V}_{w\perp} \equiv \boldsymbol{V}_{p\perp}$ (for filament segments along the present-day LOS to the pulsar) if filaments originally had strictly radial velocities (relative to the explosion center) and if there was no pre-supernova wind. In this case, $\Delta\boldsymbol{V}_{pw\perp} \equiv \boldsymbol{V}_{p\perp} - \boldsymbol{V}_{w\perp}$ vanishes and the effective transverse speed is merely the pulsar speed. (Note that we identify $\boldsymbol{V}_{m\perp}$ in eq. [8] with $\boldsymbol{V}_{w\perp}$.)

However, nonradial filament motions are expected because the pulsar's progenitor star was rotating. Even with fairly slow rotation, nonradial filament speeds of a few kilometers per second are boosted by the factor D_s/D to several thousand kilometers per second. Faster rotation yields accordingly faster transverse filament speeds today. Filaments may also have arisen from material in or deflected by a circumstellar disk around the progenitor (Fesen et al. 1992), again yielding large nonradial filament speeds today. Alternatively, the material

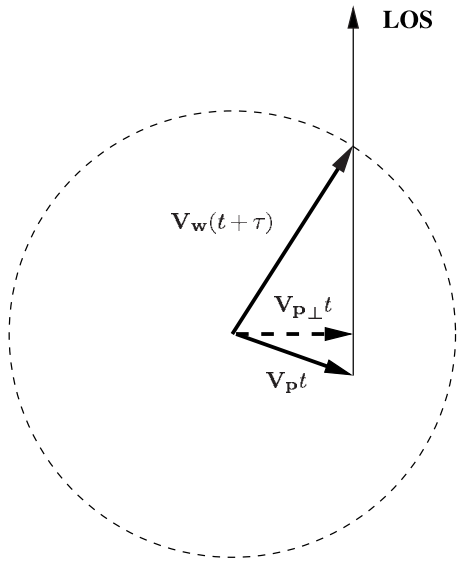

FIG. 13.—Geometry showing the LOS to the present-day location of the pulsar, which has moved a distance $\boldsymbol{V}_p t$ over the time t since the supernova explosion, while the present-day location of stellar wind material along the LOS is at a location $\boldsymbol{V}_w(t + \tau)$, taking into account an additional time τ prior to the supernova explosion during which the progenitor wind was active. Under the assumption of radial motion of the wind, the wind material (or blast wave material condensed into filaments) has a transverse speed $\boldsymbol{V}_{w\perp} = \boldsymbol{V}_{p\perp}/(1 + \tau/t)$.

responsible for scattering in the Crab Nebula could derive from the presupernova wind that occurred for a time τ prior to the explosion, as indicated in Figure 13. In any case, we assume that $\Delta V_{pw\perp}$ is nonnegligible. It is not clear if nonradial filamentary motions have been detected directly or not in the Crab Nebula (MacAlpine et al. 1994; Schaller & Fesen 2002). However, indirect constraints (Trimble 1968; see also discussion in Backer et al. 2000) based on filament motions with respect to the explosion center allow nonradial motions ~ 70 km s^{-1}.

By equating equations (7) and (8), we derive a constraint

$$\Delta V_{pw\perp} = \sqrt{2} W_C V_{\rm ISS,5/3,u} \left(\frac{D_s}{D}\right)^{1/2} \approx 18 D_s^{1/2} \text{ km s}^{-1}, \quad (9)$$

where D_s is in pc in the approximate equality. For pulsar filament distances $D_s = 1$ pc, transverse filament speeds relative to the pulsar ≈ 18 km s^{-1} are needed. We conclude that filaments that affect the pulsar's radio emission possess modest nonradial motions relative to the explosion center.

Alternatively, we can consider the combined effects of filaments in the Crab Nebula and the general ISM. We relate $V_{\rm ISS}$ to $V_{\rm ISS,5/3,u}$ using equations (10)–(18) of CR98 for a uniform ISM combined with a thin screen and find an expression analogous to equation (9),

$$\Delta V_{pw\perp} \approx \left(\frac{3}{8}\right)^{3/5} W_C V_{\rm ISS,5/3,u} \left(\frac{\rm SM_{ISM}}{\rm SM_{CN}}\right)^{3/5}, \quad (10)$$

where $\rm SM_{ISM}$ and $\rm SM_{CN}$ are the scattering measures for the general ISM and the Crab Nebula, respectively, and we have assumed that $(D_s/D)\rm SM_{ISM} \gg SM_{CN}$ but that $\rm SM_{CN} > SM_{ISM}$. The scattering measure is the LOS integral of C_n^2, the spectral coefficient for electron density irregularities (e.g., Cordes &

TABLE 4
MAXIMUM DISTANCE FOR IMPORTANCE OF NEBULAR NOISE

Telescope	ν (GHz)	G (K Jy^{-1})	$T_{\rm sys_0}$ (K)	$\epsilon^{-1/2}D_{\rm Neb}$ (kpc)
Arecibo	0.43	15	60	30
Arecibo	1.4	11	40	30
GBT	1.4	3	30	20
VLA	0.33	2	165	<5[a]
VLA	1.4	2.8	35	<2.3[a]
ATA	1.4	2.5	50	13
LOFAR	0.2	34[b]	476	20
SKA	1.4	200[c]	50	120

[a] The VLA numbers are for the D configuration, which yields the largest contribution to the system temperature from the Crab Nebula.
[b] The gain for LOFAR is that for an inner core of antennas that represents 75% of the total collecting area.
[c] The full gain of the SKA is used. In actuality, only a fraction of this gain is likely to be available for time-domain studies of pulsars.

Lazio 2002). Using values inferred for the two scattering measures (from, e.g., the electron density model, NE2001, of Cordes & Lazio 2002 and from pulse broadening of the Crab Nebula), equation (10) yields an estimate $\Delta V_{pw\perp} \approx 20$ km s^{-1}, similar to that using equation (9).

6. DETECTABILITY OF GIANT PULSES FROM EXTRAGALACTIC CRAB-LIKE PULSARS

The pulses we have identified are sufficiently strong to be detected from other galaxies. If we were to place the Crab pulsar in another galaxy, the inverse square law would lessen pulse amplitudes, but so too would it decrease the contribution to the system temperature from the Crab Nebula. Consider a Crab-like pulsar in a Crab Nebula–like nebula at distance $D_{\rm Neb}$. The system noise level for this object is (assuming it to be unresolved)

$$S_{\rm sys} = S_{\rm sys_0} + \left(\frac{D_{\rm CN}}{D_{\rm Neb}}\right)^2 S_{\rm CN}. \quad (11)$$

The nebular contribution to the system noise becomes less than a fraction ϵ of the nominal system noise if $S_{\rm sys} < (1+\epsilon)S_{\rm sys_0}$ or

$$D_{\rm Neb} > D_{\rm CN}\left(\frac{S_{\rm CN}}{\epsilon S_{\rm sys_0}}\right)^{1/2}. \quad (12)$$

Table 4 shows values of $D_{\rm Neb}$ that satisfy the inequality given by equation (12) for the Arecibo telescope, the Green Bank Telescope (GBT), the VLA (and the extended VLA), the Allen Telescope Array, LOFAR, and the SKA. In all cases, we assume that the nebula is unresolved. For the VLA, the ATA, LOFAR, and some designs for the SKA, this assumption will break down. For $\epsilon = 1$ (equal contributions to $S_{\rm sys}$ from the nebula and from receiver and background noise), the nebula is unimportant for objects in the Magellanic Clouds for either of the existing telescopes. However, for the SKA, nebular noise is dominant for such objects. For the largest nearby spiral galaxies (M31 and M33), however, nebular noise is negligible for all existing and contemplated telescopes.

The optimal frequency can also be determined. If we assume that the spectrum is the same as that of the Crab pulsar, lower frequencies are favored unless propagation effects smear the pulse. For the Crab pulsar itself, 0.43 GHz is approximately the lowest frequency at which propagation effects are sufficiently small to allow detection of many giant pulses. For pulsars in M31 or M33, the dispersion measures expected given their respective Galactic latitudes and inclinations are approximately equal to the DM of the Crab pulsar. Similarly, the scattering is expected to be approximately the same. Consequently, we can use our 0.43 GHz results on the Crab pulsar to estimate the S/N expected for extragalactic emitters of giant pulses.

The strongest pulse observed at 0.43 GHz has $\rm S/N_{max} = 1.1\times10^4$ even with the system noise dominated by the Crab Nebula. For objects in M31 ($D \approx 0.8$ Mpc) or further, the system noise is essentially unaffected by the nebular contribution. If the Crab pulsar were not embedded in its nebula, the S/N of our largest pulse would have been $S_{\rm CN}/S_{\rm sys_0} \approx 300$ times larger, or 3.3×10^6. For this particular pulse, the maximum distance it could be detected at a specified S/N, $(\rm S/N)_{det}$, is

$$D_{\rm max} = D_{\rm CN}\left[\frac{(\rm S/N)_{max}}{(\rm S/N)_{det}}\left(1+\frac{S_{\rm CN}}{S_{\rm sys_0}}\right) - \frac{S_{\rm CN}}{S_{\rm sys_0}}\right]^{1/2} \quad (13)$$

$$\approx 1.6\ {\rm Mpc}\left[\frac{(\rm S/N)_{det}}{5}\right]^{-1/2}. \quad (14)$$

The largest 0.43 GHz pulse would thus be detectable from M33 ($D \approx 0.93$ Mpc) using the Arecibo telescope and our current spectrometer at $\rm S/N \approx 15$. Using the GBT to observe M31 (since M31 is outside the declination range of Arecibo), our largest pulse would have $\rm S/N \approx 4.8$. Thus, a convincing detection of giant pulses from M31 with the GBT would require longer dwell times than 1 hr in order that yet stronger pulses could be detected. Detection of giant pulses is discussed in general in Cordes & McLaughlin (2003) and in particular from nearby galaxies in McLaughlin & Cordes (2003).

LOFAR would allow detection of a giant pulse at 0.2 GHz at the 5 σ level out to a distance of 1.5 Mpc for our largest pulse at 0.43 GHz, scaled to 0.2 GHz. The SKA would yield $D_{\rm max} \approx 5.9$ Mpc for a 5 σ detection of our largest pulse at 0.43 GHz. There are approximately 16 galaxies (of M33's size or larger) within this distance. If pulsars like the Crab pulsar persist in emitting giant pulses for a time of order the current age of the Crab ($\sim10^3$ yr) and if the birth rate of pulsars scales as the ratio of a galaxy's mass to the Milky Way's mass, $\dot{N}_{\rm psr} \approx (10^{-2}\ {\rm yr}^{-1})M_{\rm gal}/M_{\rm MW}$, we expect that there should be a few to about 20 such pulsars in each of these galaxies. Of course, giant pulses are also emitted by millisecond pulsars whose magnetic fields at their light cylinders are comparable to that of the Crab pulsar (Cognard et al. 1996; Romani & Johnston 2001; Johnston & Romani 2002), so the numbers of detectable objects may be larger. At present, however, the Crab pulsar emits the most luminous giant pulses of any of these objects and best serves as a prototype for detectable objects from other galaxies.

7. SUMMARY AND CONCLUSIONS

We have shown that giant pulses from the Crab pulsar are restricted to only two of the pulse components seen in long-term average profiles. These components are the same as those detected at optical, X-ray, and gamma-ray energies, suggesting that the mechanism for giant-pulse emission occurs high in

the magnetosphere, where these emissions are expected to originate. The alignment of the radio components with high-energy components is good to at least 0.05 cycles, or about 1.7 ms, indicating that the emission regions are colocated in altitude to within this light-travel distance. Apart from these constraints on relative localizations, our data do not provide any independent absolute constraints on the location of emission regions.

The occurrence of giant pulses is strongly frequency dependent. We find that giant pulses "follow" the interpulse in pulse phase as it shifts to earlier phases above $\sim$4 GHz. We therefore conclude that the same physical region produces both the low-frequency and the shifted, high-frequency interpulse. While the main pulse is dominant from 0.43 to 5.5 GHz, in both the average profiles and the number of giant pulses, at 8.8 GHz the interpulse is dominant. We have no clear interpretation of this trend other than the usual suspect processes: beaming and spectral dependence. It is our aim to analyze the profile shapes and giant-pulse occurrence histograms along with multiwavelength pulse profiles extending to greater than 100 MeV gamma rays in order to better constrain the roles of beaming and coherence mechanisms. This work will be deferred to another paper.

Epoch dependence of the giant-pulse rate derives from scintillation effects that appear to be strongly influenced by plasma in the Crab Nebula. Backer et al. (2000) demonstrate that multiple images occur as a result of the passage across the LOS of refracting plasma. We establish the scintillation timescale that is sufficiently short ($\sim$25 s at 1.48 GHz) that plasma relatively near the pulsar (i.e., inside the Crab Nebula) is required. Our analysis on giant-pulse amplitudes suggests that, to the extent that the Crab pulsar serves as a prototype of giant-pulse emission, giant pulses from extragalactic pulsars should be detectable out to large distances $\sim$1.6 Mpc at Arecibo with existing back-end spectrometers.

We thank Bill Sisk and Jeff Hagen for developing the WAPP system at the Arecibo Observatory, which was crucial for providing the data analyzed in this paper. We thank Mal Ruderman for helpful discussions. N. D. R. B. is supported by an MIT-CfA Postdoctoral Fellowship at Haystack Observatory. Work at Cornell University was supported by NSF grants AST 98-19931 and 02-06036. M. A. M. was also supported by an NSF MPS-DRF Fellowship. This work was also supported by the National Astronomy and Ionosphere Center, which operates the Arecibo Observatory under a cooperative agreement with the NSF. T. H. H. thanks NAIC for partial sabbatical leave support during this work.

APPENDIX

FREQUENCY STRUCTURE FROM SCINTILLATING AMPLITUDE-MODULATED, POLARIZED SHOT NOISE

Frequency structure in the radio spectrum of a single pulse is caused by both the statistical properties of the pulsed radiation at the time of emission and the interference effects of multipath propagation. A model that suffices to describe many aspects of pulsar radiation is the amplitude-modulated noise model (Rickett 1975) augmented to include polarized shot-noise statistics (Cordes 1976): the amplitude-modulated, polarized shot-noise (AMPSN) model. Frequency structure of single pulses was discussed by Cordes & Hankins (1979) in terms of the AMPSN model for B0950+08. Here we amplify their treatment to show the interplay of intrinsic and interference effects on the frequency structure. We thus develop the SAMPSN model.

Recent results (Hankins et al. 2003) imply that the Crab pulsar's giant pulses are indeed comprised of individual shot nanopulses, in conformance with the AMPSN model. Let $\epsilon_e(t)$ be the complex, narrowband electric field emitted at the pulsar and selected by the receiving system and mixed to baseband (see, e.g., Rickett 1975; Cordes 1976). We consider, for now, just a single polarization channel. For an individual giant pulse, we describe ϵ_e as an ensemble of N_s shot pulses having individual amplitudes, a_j, but (for simplicity) identical shapes, $\Delta(t)$:

$$\epsilon_e(t) = \sum_{j=1}^{N_s} a_j \Delta\left(t - t_j\right). \tag{A1}$$

The width of $\Delta(t)$ is the reciprocal of the receiver bandwidth used to form $\epsilon(t)$. The corresponding shot pulse at the original radio frequency has width $\sim\nu_{\rm RF}^{-1}$ $\sim$0.1–2 ns for our data. Each shot pulse reaches the observer along N_p paths as a result of multipath propagation between the pulsar and Earth. Each path has an associated time delay δt_p and amplitude g_k. The set of paths changes on a timescale that we assume is much longer than a single spin period. In addition, all propagation quantities (N_p, δt_p, and g_k) are strong functions of frequency because the refractive index is that for a cold plasma. Using the total propagation time, $D/c + \delta t_p$, the received electric field is

$$\epsilon(t) \propto \sum_{j=1}^{N_s} a_j \sum_{k=1}^{N_p} g_k \Delta\left(t - t_j - D/c - \delta t_{pk}\right). \tag{A2}$$

Here we have ignored delays from dispersive propagation through the ISM because they are deterministic and correctable. Denoting a Fourier transform with a tilde and using the shift theorem, we find that the instantaneous spectrum is

$$I(\nu) \equiv |\tilde{\epsilon}(\nu)|^2 \propto \left|\tilde{\Delta}(\nu)\right|^2 A(\nu) G(\nu), \tag{A3}$$

where ν is the baseband frequency and

$$A(\nu) = \left| \sum_{j=1}^{N_s} a_j e^{-2\pi i \nu t_j} \right|^2, \tag{A4}$$

$$G(\nu) = \left| \sum_{k=1}^{N_p} g_j e^{-2\pi i \nu \delta t_{pk}} \right|^2. \tag{A5}$$

In the limit of large N_s and N_p, we expect Gaussian statistics for the sums in the equations for A and G. Consequently, A and G will both have exponential statistics, for which $\langle A^2 \rangle / \langle A \rangle^2 = \langle G^2 \rangle / \langle G \rangle^2 = 2$. As is well known in the scintillation literature (e.g., Rickett 1990), scintillation fluctuations in the strong scattering regime have exponential statistics for a point source if there is no bandwidth smoothing. Note that our formulation of amplitude-modulated noise differs from that of Rickett (1975) and Cordes (1976), who model the emitted signal as $\epsilon_e(t) = a(t)m(t)$, where $a(t)$ is an envelope function that modulates the noise process $m(t)$. Instead, the envelope function is absorbed into the particular distribution of emission times, t_j.

To isolate the frequency structure of $A(\nu)$ from $G(\nu)$, one must take into account their characteristic timescales. It is reasonable to assume that the pattern of shot pulses in $\epsilon(t)$ does not repeat. On a physical basis, such shot pulses may result from the sweep of relativistic beams through the LOS, or they may represent bona fide temporal modulations. Either way, on timescales $\gtrsim P/2\pi$ (P is the pulsar period), we expect the relativistic plasma flow in the pulsar magnetosphere to have reorganized completely. The scintillation pattern, on the other hand, is sustained. It is usually true for pulsars that if the scintillation frequency structure is resolved by the spectrometer, it persists over timescales of seconds to hours, depending on the pulsar and frequency. For heavily scattered pulsars, the frequency structure is too fine to resolve and the scintillation time is accordingly short. Thus, for most pulsars, the frequency structure in $G(\nu)$, if resolved, is characterized by averaging $I(\nu)$ over many individual pulses and then performing a correlation analysis to determine the characteristic bandwidth.

For the Crab pulsar, which emits giant pulses only sporadically, it is more difficult to separate $A(\nu)$ from $G(\nu)$ and also estimate the scintillation timescale. For an individual giant pulse, $A(\nu)$ and $G(\nu)$ both contribute to the observed frequency structure, with similar statistics. However, the characteristic width of $G(\nu)$ scales strongly with frequency, as discussed above, while $A(\nu)$ is associated with the temporal widths of the giant pulses and may be less frequency dependent.

A1. STATISTICS FOR A SINGLE POLARIZATION CHANNEL

Some useful statistics of the SAMPSN model are as follows. The modulation index of the spectrum $I(\nu)$ is $\sigma_I / \langle I \rangle = 3$ when A and G both have exponential statistics. For a pair of pulses for which $A(\nu)$ has decorrelated completely while $G(\nu)$ is perfectly correlated, we expect the cross-correlation to be $\rho_{12} = \langle \delta I_1(\nu) \delta I_2(\nu) \rangle / \sigma_I^2 = \frac{1}{3}$. The correlation coefficient will decline to zero on a time lag between the pair of pulses determined by the characteristic scintillation time, defined as the lag at which the correlation coefficient is e^{-1} of its maximum value of $\frac{1}{3}$.

The autocorrelation function (ACF) of the spectra for single pulses can be written in the form

$$R(\delta\nu) = \langle I(\nu) I(\nu + \delta\nu) \rangle = R_{|\tilde{\Delta}|^2}(\delta\nu) R_A(\delta\nu) R_G(\delta\nu). \tag{A6}$$

$R_{|\tilde{\Delta}|^2}(\delta\nu)$ is a broad function that is the ACF of the bandpass filter used to form $\epsilon(t)$, while R_A and R_G can be much narrower and are of the form $R_X(\delta\nu) = \langle X \rangle^2 [1 + m_X^2 \rho_X(\delta\nu)]$, where $m_X = 1$ for exponential statistics and $\rho_X(0) = 1$. The intensity correlation function,

$$R(\delta\nu) = \langle G \rangle^2 \langle A \rangle^2 R_{|\tilde{\Delta}|^2}(\delta\nu) \left[1 + m_A^2 \rho_A(\delta\nu)\right] \left[1 + m_G^2 \rho_G(\delta\nu)\right], \tag{A7}$$

will typically have a narrower component and a broader component associated with ρ_A and ρ_G, respectively, or vice versa. The total squared modulation index is $m^2 = \sigma_I^2 / \langle I \rangle^2 = R(0) / \langle G \rangle^2 \langle A \rangle^2 R_{|\tilde{\Delta}|^2}(0) - 1 = 1 + m_A^2 + m_G^2 = 3$. If the data are channelized with channel bandwidths larger than the characteristic bandwidth of A or G, the modulation index will be reduced.

Some giant pulses comprise a small number of shot pulses, $N_s \approx$ few, in which case $A(\nu)$ will have nonexponential statistics. For example, for two equal-amplitude shot pulses separated by Δt_{12}, $A(\nu) \propto (1 - \cos 2\pi\nu\Delta t_{12})$. If $\nu \Delta t_{12} \gg 1$, we would have $m_A = 2^{-1/2}$ and the spectral shape would be oscillatory. In the limit of a single shot pulse (or a cluster of shot pulses contained within an interval smaller than the reciprocal bandwidth), the modulation across the bandwidth would derive solely from G, the scintillation factor.

A2. STATISTICS FOR THE TOTAL INTENSITY

When two polarization channels are summed to yield the total intensity, as in the analysis of this paper, the statistics are altered. Scintillations are identical for the two polarizations, while the frequency structure from the AMPSN will differ according to the degree of polarization. If the signal is 100% polarized, the total intensity will have the same statistics as that of a single polarization channel containing the signal, while for an unpolarized signal, the AMPSN spectral fluctuations will be reduced by $\sqrt{2}$.

Letting d_p equal the total degree of polarization (linear and circular), it may be shown (Cordes 1976) that the intensity modulation index is now (in the limit of Gaussian statistics for a single polarization channel)

$$m_I^2 = m_G^2 + \left(1 + m_G^2\right)\left(1 + d_p^2\right)/2m_G = 1 = 2 + d_p^2, \tag{A8}$$

where the last equality holds for $m_G = 1$. Now, when the total intensity spectra of pulse pairs are cross-correlated, we have

$$\rho_{12} = \langle \delta I_1(\nu)\delta I_2(\nu)\rangle/\sigma_I^2 = \frac{m_G^2}{m_G^2 + \left(1 + m_G^2\right)\left(1 + d_p^2\right)/2} m_G = 1 = \frac{1}{2 + d_p^2}. \tag{A9}$$

REFERENCES

Allen, C. W. 1973, Astrophysical Quantities (3rd ed.; London: Athlone)
Argyle, E., & Gower, J. F. R. 1972, BAAS, 4, 216
Backer, D. C., Wong, T., & Valanju, J. 2000, ApJ, 543, 740
Backer, D. C., Wong, T., Valanju, J., & Lyne, A. 1998, BAAS, 30, 1151
Bhat, N. D. R., Cordes, J. M., & Chatterjee, S. 2003, ApJ, 584, 782
Bietenholz, M. F., Kassim, N., Frail, D. A., Perley, R. A., Erickson, W. C., & Hajian, A. R. 1997, ApJ, 490, 291
Caraveo, P. A., & Mignani, R. P. 1999, A&A, 344, 367
Cognard, I., Shrauner, J. A., Taylor, J. H., & Thorsett, S. E. 1996, ApJ, 457, L81
Cordes, J. M. 1976, ApJ, 210, 780
Cordes, J. M., & Hankins, T. H. 1979, ApJ, 233, 981
Cordes, J. M., & Lazio, T. J. W. 2001, ApJ, 549, 997
———. 2002, preprint (astro-ph/207156)
Cordes, J. M., & McLaughlin, M. A. 2003, ApJ, 596, 1142
Cordes, J. M., & Rickett, B. J. 1998, ApJ, 507, 846 (CR98)
Cordes, J. M., Weisberg, J. M., & Boriakoff, V. 1985, ApJ, 288, 221
Fesen, R. A., & Kirshner, R. P. 1982, ApJ, 258, 1
Fesen, R. A., Martin, C. L., & Shull, J. M. 1992, ApJ, 399, 599
Hankins, T. H., Kern, J. S., Weatherall, J. C., & Eilek, J. A. 2003, Nature, 422, 141
Hankins, T. H., & Moffett, D. A. 1998, BAAS, 30, 903
Isaacman, R., & Rankin, J. M. 1977, ApJ, 214, 214
Johnston, S., & Romani, R. W. 2002, MNRAS, 332, 109
Löhmer, O., Kramer, M., Mitra, D., Lorimer, D. R., & Lyne, A. G. 2001, ApJ, 562, L157
Lundgren, S. C., Cordes, J. M., Ulmer, M., Matz, S., Lomatch, S., Foster, R. S., & Hankins, T. 1995, ApJ, 453, 433
Lyne, A. G., Pritchard, R. S., & Graham-Smith, F. 2001, MNRAS, 321, 67
Lyne, A. G., & Thorne, D. J. 1975, MNRAS, 172, 97
MacAlpine, G. M., et al. 1994, ApJ, 432, L131
McLaughlin, M. A., & Cordes, J. M. 2003, ApJ, 596, 982
Moffett, D. A., & Hankins, T. H. 1996, ApJ, 468, 779
Narayan, R. 1992, Philos. Trans. R. Soc. London A, 341, 151
Rickett, B. J. 1975, ApJ, 197, 185
———. 1990, ARA&A, 28, 561
Romani, R. W., & Johnston, S. 2001, ApJ, 557, L93
Sallmen, S., Backer, D. C., Hankins, T. H., Moffett, D., & Lundgren, S. 1999, ApJ, 517, 460
Sankrit, R., et al. 1998, ApJ, 504, 344
Schaller, E. L., & Fesen, R. A. 2002, AJ, 123, 941
Staelin, D. H., & Reifenstein, E. C. 1968, Science, 162, 1481
Trimble, V. 1968, AJ, 73, 535